Plasmonics (2025) 20:10489–10498
https://doi.org/10.1007/s11468-025-03119-9

RESEARCH

Double-Groove ZnO–Au Photonic Quasi-crystal Fiber Surface Plasmon Resonance Sensor

Qiang Liu[1] · Xinrui Li[1] · Li Liu[2] · Kaiyu Wang[1] · Yudan Sun[3] · Xiaoxu Zhang[1] · Wei Liu[1] · Jingwei Lv[1] · Xueyan Zhao[1] · Paul K. Chu[4] · Chao Liu[1]

Received: 23 April 2025 / Accepted: 11 June 2025 / Published online: 27 June 2025

Abstract

A photonic quasi-crystal fiber surface plasmon resonance (PQF-SPR) sensor composed of a ZnO–Au bilayer film is designed and analyzed. The dual-core groove structure is designed to improve the performance of the sensor. The finite element method is performed to analyze the influence of the groove shape on the sensing properties. The results reveal that the shape of the groove directly influences the coupling between the core mode and the surface plasmon polariton (SPP) mode as well as the peak loss and full-width at half-maximum (FWHM) of the loss spectra. By optimizing the groove shape and structural parameters of the PQF, a maximum wavelength sensitivity of 25,000 nm/RIU and a quality factor (figure of merit) of 432 RIU^{-1} are attained in the refractive index range between 1.30 and 1.41. This study provides valuable insights and guidance for the development and optimization of high-performance SPR sensors.

Keywords PQF-SPR sensor · Surface plasmon resonance · Photonic quasi-crystal fiber · ZnO–Au composite film

Introduction

Surface plasmon resonance (SPR) results from the collective oscillation of electrons induced by photons which then excite surface plasmon polariton (SPP) waves [1, 2]. The SPR effect can be utilized to design highly sensitive refractive index sensors. The traditional SPR refractive index sensor typically employs a prism structure, but the large size and complex configuration restrict its application field [3]. In order to overcome these limitations, optical fibers as carriers have been considered in the design of surface plasmon resonance sensors, for example, refractive index sensors based on single-mode and multi-mode optical fibers [4–6], but they tend to have low sensitivity. In contrast, SPR sensors based on photonic crystal fibers (PCF) and photonic quasi-crystal fibers (PQF) have gained significant attention due to their better sensing characteristics and flexible structures. The application field is further expanded, such as biomedical field [7–9], gas and liquid analytes of industry field [10–14].

Similar to Bloch surface waves based sensor [15–19], the properties of PCF-SPR and PQF-SPR sensors mainly depend on the material and structure. In addition, the algorithms such as machine learning, genetic algorithms are also used to optimize the sensor [20]. Common plasmonic materials are gold, silver, copper, and graphene [21–24], and metal oxides such as zinc oxide (ZnO) and titanium dioxide (TiO_2) have also been found to yield good sensitivity and figure of merit (FOM) [25]. Different PCFs with D-shape [26, 27], groove-shape [28, 29], eccentric [30], dual-core [31, 32], and multi-core [33] configurations have been proposed. The objective is to enhance the coupling between the core mode and the SPP mode by adjusting the position of the fiber core and plasmonic materials. For example, the D-shape structures have been widely studied due to the better sensing performance [34–36]. Recently, the similar groove-shape structures attract the interest of researchers. Rahman et al. [37] have proposed a U-shape groove structure

✉ Chao Liu
msm-liu@126.com

1 School of Physics and Electronic Engineering, Northeast Petroleum University, Daqing 163318, China

2 No. 5 Oil Production Plant of Daqing Oilfield Co., Ltd., Daqing 163513, China

3 College of Mechanical and Electrical Engineering, Daqing Normal University, Daqing 163712, China

4 Department of Physics, Department of Materials Science and Engineering, and Department of Biomedical Engineering, City University of Hong Kong, Tat Chee Avenue, Kowloon, Hong Kong, China

with a maximum wavelength sensitivity of 25,000 nm/RIU and FOM of 277.77 RIU^{-1}. Islam et al. [38] have designed a single-core double-sided groove structure comprising gold with peak wavelength sensitivity and FOM of 7000 nm/RIU and 94.97 RIU^{-1}, respectively. Gao et al. [39] have studied a single-core double-sided groove structure based on the D-type PCF by utilizing the relationship between temperature and refractive index of the medium to measure the temperature. Majeed et al. [40] have developed a double-sided groove PCF-SPR refractive index sensor using a rectangular hole design, which shows a wavelength sensitivity of 33,000 nm/RIU by controlling the air hole size between the fiber core and plasmonic material. Mittal et al. [41] have proposed an eccentric groove structure incorporating the composite film of Au- $_2$, and the wavelength sensitivity and amplitude sensitivity are 2000 nm/RIU and 374.06 RIU^{-1}, respectively. Dai et al. [42] have introduced a TiO_2-Au composite film into the PCF-SPR sensor, and the quasi-D-type PCF with a U-shape groove exhibits a wavelength sensitivity of 7500 nm/RIU and FOM of 634.1 RIU^{-1} in the analysis of hemoglobin solutions. Liu et al. [43] have constructed a D-type PQF-SPR methane sensor with a groove structure, in which ZnO and Au are deposited on the groove surface to form a composite film for methane detection. These previous studies reveal that a groove structure can enhance the properties of SPR sensors. However, there has been no discussion on the impact of the groove parameter on the sensing characteristics. In this work, a novel dual-core, dual-sided groove PQF-SPR sensor with a ZnO–Au composite film is designed, and the effects of the groove shape on the sensor are analyzed systematically for the first time. By optimizing the sensor structure, a maximum wavelength sensitivity of 25,000 nm/RIU in the refractive index range of 1.30–1.41 and the optimal FOM of 432 RIU^{-1} are achieved.

Structure and Analysis

The sensor has the six-fold Penrose photonic quasi-crystal structure shown in Fig. 1b. The upper and lower eight air holes indicated by the dashed lines are removed, and then two air holes with a diameter of $d_2 = 1.3$ μm are added to form two fiber cores. The distance h_1 between the two air holes and the fiber center is 3.3 μm. Figure 1a illustrates the dual-core structure. The diameter of the eight large outer air holes is $d_3 = 2.4$ μm, and the distance of these air holes is $\Lambda = 3.3$ μm. The diameter of the central air hole is $d_1 = 1$ μm, and two air holes with a diameter of d_2 are located at a distance of $\Lambda/2$ from the fiber center. The designed PQF can be manufactured by the computer assisted capillary arrangement or 3D printing preform technology [44, 45]. The symmetrical dual-sided groove with $h = 5.05$ μm is manufactured by the femtosecond laser micromachining or focused ion beam (FIB) milling [46]. Finally, the gold (Au) and zinc oxide (ZnO) films with thicknesses of $t_1 = 0.035$ μm and $t_2 = 0.005$ μm are deposited sequentially on the groove surface by the physical vapor deposition (PVD) and chemical vapor deposition (CVD), respectively [47, 48]. The green part of the structure represents the measured medium. The finite element method (FEM) is employed to analyze the characteristics of the sensor. In the simulation, the geometry is broken up into smaller portions, and a wave equation with suitable boundary conditions is solved for each section. An extremely fine mesh element controlled by physics is utilized to produce the most accurate simulation results. The complete mesh consists of 77,800 domain elements and 6895 boundary elements. In order to absorb radiation, an additional cylindrical type of perfectly matched layer (PML) is added to the PQF-SPR sensor's outermost layer [49].

The sensor is composed of silicon dioxide, and the dispersion relation is described by the Sellmeier equation [50]:

$$n(\lambda) = \sqrt{1 + \frac{0.6961663\lambda^2}{\lambda^2 - 0.0684043^2} + \frac{0.4079426\lambda^2}{\lambda^2 - 0.1162414^2} + \frac{0.8974794\lambda^2}{\lambda^2 - 9.896161^2}}, \quad (1)$$

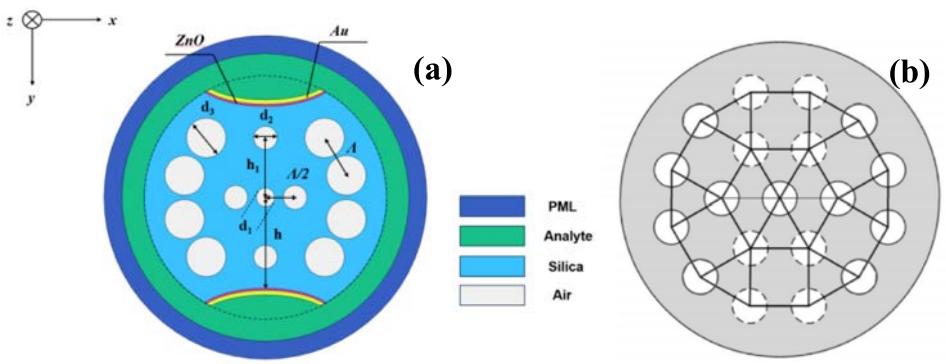

Fig. 1 **a** Cross-section of the PQF-SPR sensor and **b** Six-fold Penrose photonic quasi-crystal structure

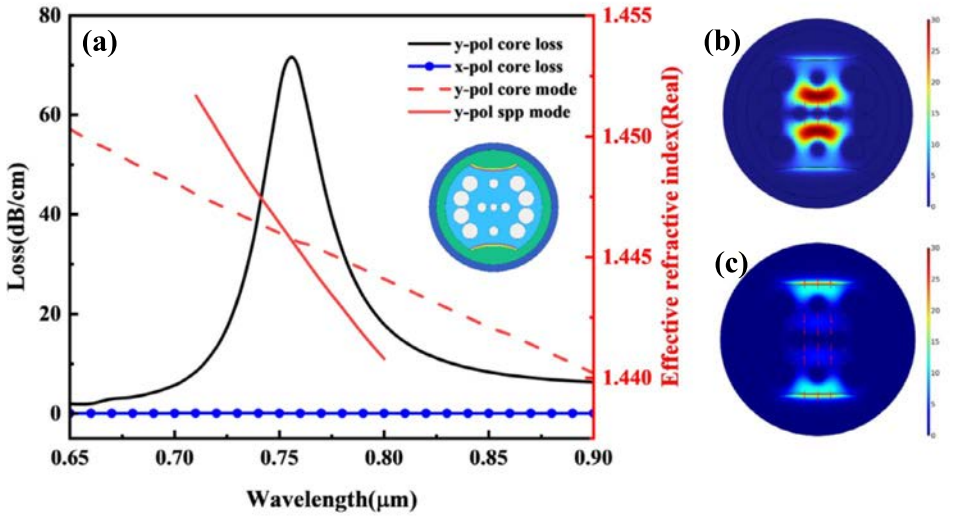

Fig. 2 Dual-core groove structure (**a**) loss spectra and dispersion curves, (**b**) electric field diagram of the y-polarized core mode, and (**c**) electric field diagram of the y-polarized SPP mode at the phase matching point

where λ represents the wavelength of the incident light in vacuum with a unit of micrometer. The dielectric constant of gold can be derived from the Drude-Lorentz model [51]:

$$\varepsilon_{Au}(\omega) = \varepsilon_{\infty} - \frac{{\omega_p}^2}{\omega^2 + \mathrm{i}\omega\omega_{\tau}}, \tag{2}$$

where $\omega_p = 1.36 \times 10^{16}$ (rad/s) and $\omega_{\tau} = 1.45 \times 10^{14}$ (rad/s) represent the plasma frequency and the scattering frequency of electrons in the gold film, respectively. The dielectric constant ε_{∞} at high frequencies is 9.75, $\omega = 2\pi c/\lambda$ denotes the angular frequency of the incident light, ε_{Au} refers to the complex dielectric constant of the gold film. The dielectric property of ZnO is calculated by Eq. (3) [52] and λ is operating wavelength in μm.

$$\varepsilon_{ZnO}(\lambda) = 2.81418 - \frac{\lambda^2 0.87968}{(\lambda^2 - 0.3042^2) - 0.00711^2}, \tag{3}$$

The properties of the PQF-SPR sensor are typically determined by calculating the confinement loss of the core mode. As the real parts of the effective refractive indexes of the core fundamental mode and the surface plasmon polariton (SPP) mode are equal, SPR occurs on the metal surface. The coupling between the core mode and the SPP mode increases the loss of the core mode as shown below [53]:

$$\alpha_{CL}(dB/cm) = \frac{20}{\ln(10)} \times \frac{2\pi}{\lambda} \times \mathrm{Im}(n_{eff}) \times 10^4, \tag{4}$$

where $\mathrm{Im}(n_{eff})$ is the imaginary part of the effective refractive index of the core mode at different wavelengths.

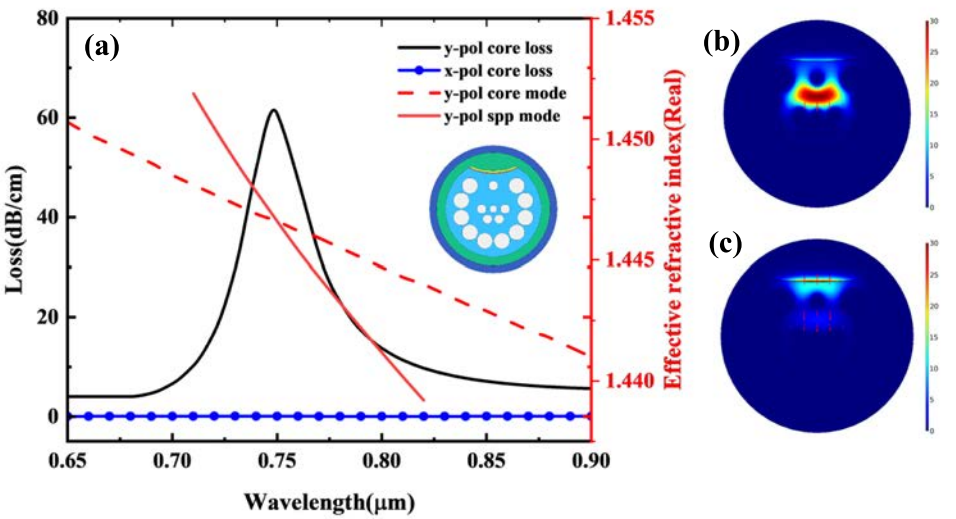

Fig. 3 Single-core groove structure (**a**) loss spectra and dispersion curves, (**b**) electric field diagram of the y-polarized core mode, and (**c**) electric field diagram of the y-polarized SPP mode at the phase matching point

Using 1.39 as the refractive index of the medium, the real parts of the effective refractive indexes of the y-polarized core mode and SPP mode are calculated using FEM and shown by the red dashed line and red solid line in Fig. 2a. The intersection of the two curves means that the phase-matching condition is satisfied, and the core mode is coupled with the SPP mode as shown in Fig. 2b and c. Consequently, the partial core mode energy couples to the ZnO–Au composite film. The loss spectrum of the y-polarized core mode shows a peak indicated by the solid black line in Fig. 2a. Similarly, the loss spectrum of the x-polarized core mode is calculated and shown by the blue solid line, the loss peak is significantly lower than that of the y-polarized core mode. In order to highlight the advantage of dual-core groove structure, the loss spectrum of single-core groove structure is also calculated as shown in Fig. 3. It can be seen that the spectrum exhibit lower peak and wider linewidth. It means that the performance of single-core groove structure is relatively poor. Therefore, the y-polarized core mode of dual-core groove structure is selected in our subsequent analysis.

The sensitivity of the PQF-SPR sensor can be evaluated by the wavelength sensitivity and amplitude sensitivity. The wavelength sensitivity is determined by the peak wavelength shift $\Delta\lambda_p$ in the loss spectrum. It stems from the refractive index variation Δn_a of the measured medium as shown below [54]:

$$S_w(nm/RIU) = \frac{\Delta\lambda_p}{\Delta n_a}. \tag{5}$$

The wavelength resolution of the sensor is defined as follows [55]:

$$R = \frac{\Delta n_a \times \Delta\lambda_{\min}}{\Delta\lambda_p}, \tag{6}$$

where $\Delta\lambda_{min}$ represents the minimum wavelength resolution of the wavelength demodulator, which can be set to 0.1 nm. The full-width at half-maximum (FWHM) of the loss spectrum impacts the resolution and signal-to-noise ratio (SNR) of the sensor. The detection accuracy can be evaluated according to the figure of merit (FOM) defined below [56]:

$$\mathrm{FOM}(RIU^{-1}) = \frac{S_w}{\mathrm{FWHM}}. \tag{7}$$

Equation (7) discloses that a wavelength sensitivity and smaller FWHM translate into better sensing characteristics.

The amplitude sensitivity is based on the following [57]:

$$S_a(RIU^{-1}) = -\frac{1}{\alpha_{CL}} \times \frac{\Delta\alpha_{CL}}{\Delta n_a} \tag{8}$$

where $\Delta\alpha_{CL}$ defines the confinement loss variation and α_{CL} is the loss in the initial state.

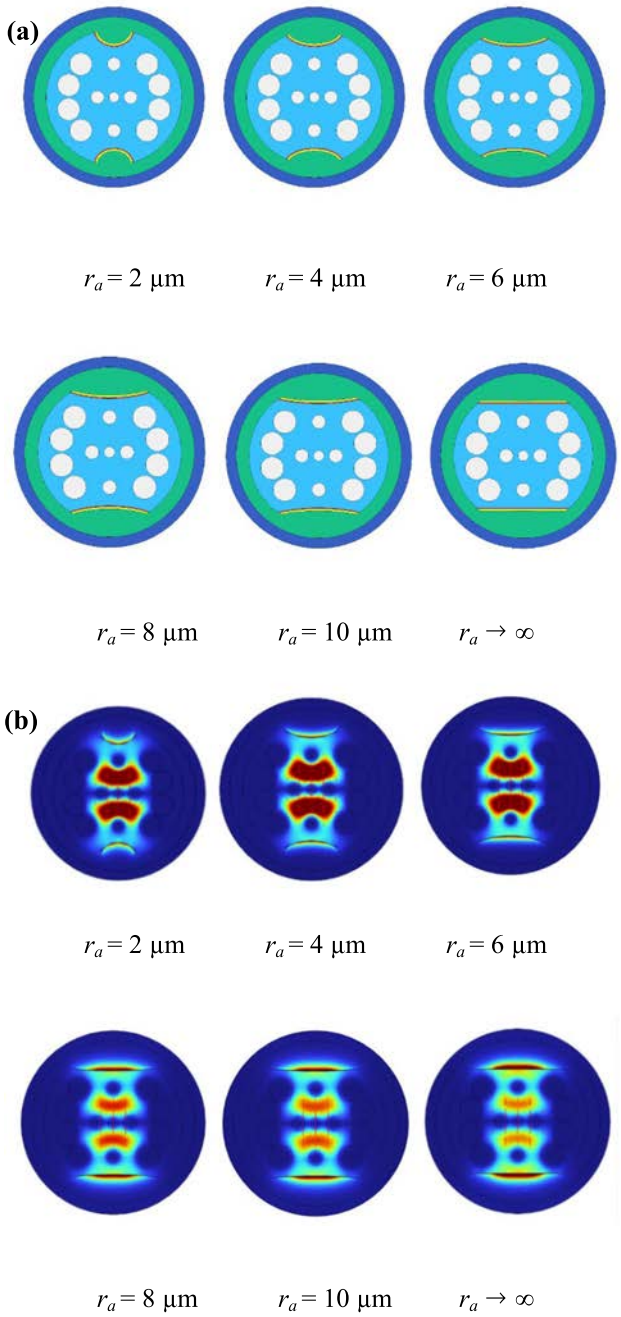

Fig. 4 **a** Schematic diagrams of the structure of the sensors with different long semi-major axis r_a and **b** Electric field distributions of the y-polarized core mode

Optimization and Discussion

The effects of the shape of the grooves on the sensing are assessed. The ellipse with a long semi-axis r_a and a short semi-axis r_b is adopted to form the groove. The long axis of the ellipse is parallel to the x-axis. The short semi-axis is fixed at r_b = 1.7 μm, and the distance h is 5.05 μm. As the

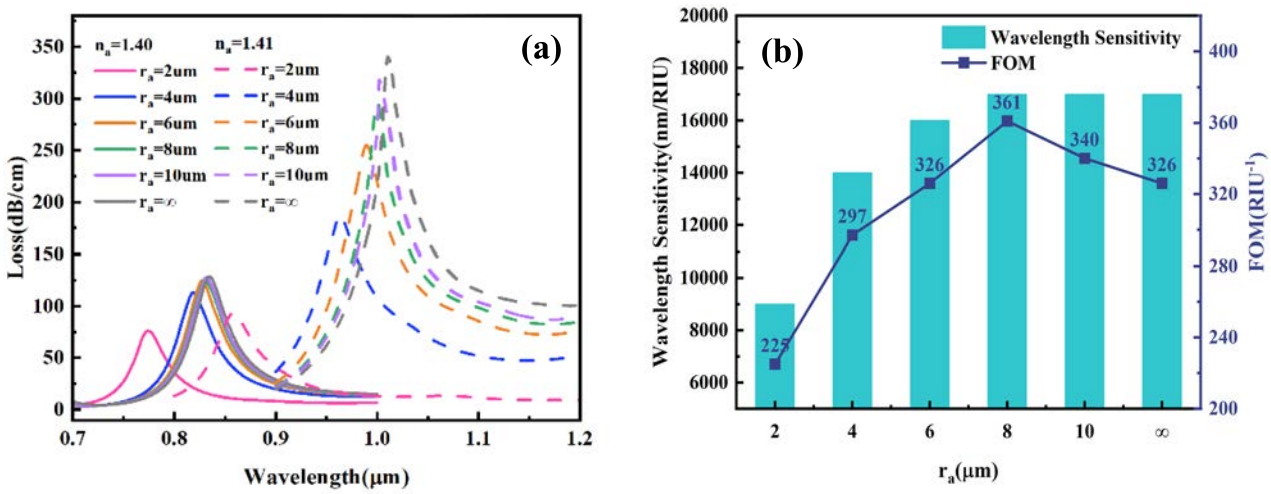

Fig. 5 **a** Loss spectra and **b** wavelength sensitivity and FOM for different r_a

long semi-axis r_a are 2 μm, 4 μm, 6 μm, 8 μm, 10 μm, and ∞, the structures are shown in Fig. 4a. The corresponding mode field diagrams of the y-polarized core mode are shown in Fig. 4b for $n = 1.40$ as Au and ZnO thicknesses are $t_1 = 35$ nm and $t_2 = 5$ nm, respectively. It can be seen that the shape of the groove directly influences the distribution and intensity of the electric field. With increasing semi-major axis r_a of the ellipse, the SPR effect becomes progressively stronger. The intensity of the y-polarized core mode decreases as the SPP mode field expands. It is because the area of the plasmonic substance expands with increasing r_a and the plasmonic medium is closer to the fiber core. As a result, the coupling between the core mode and the SPP mode becomes stronger, and the peaks of the loss spectra increase gradually.

Figure 5a depicts the loss spectra of the y-polarized core mode for different r_a as the refractive index is changed from 1.40 to 1.41. For a fixed refractive index, the peak in the loss spectrum rises and shifts towards a longer wavelength with increasing r_a. Figure 5b exhibits the wavelength sensitivity and FOM. When r_a is small, the wavelength sensitivity of the sensor is low. When $r_a \geq 8$ mμ, the shape of the groove changes slightly, the wavelength sensitivity remains nearly unchanged. But it still influences the coupling between the core mode and SPP mode, and results in larger linewidth of the loss spectrum which gives rise to a smaller FOM. To achieve the optimal sensing performance, $r_a = 8$ μm is selected.

The effects of the thickness of the ZnO–Au composite film are then investigated. For a ZnO film thickness t_2 of

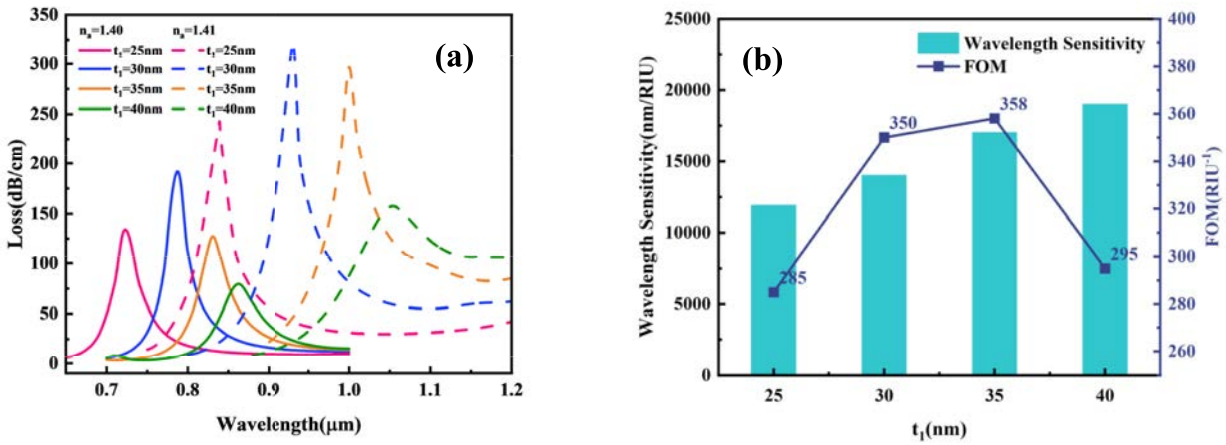

Fig. 6 **a** Loss spectra and **b** wavelength sensitivity and FOM for different t_1

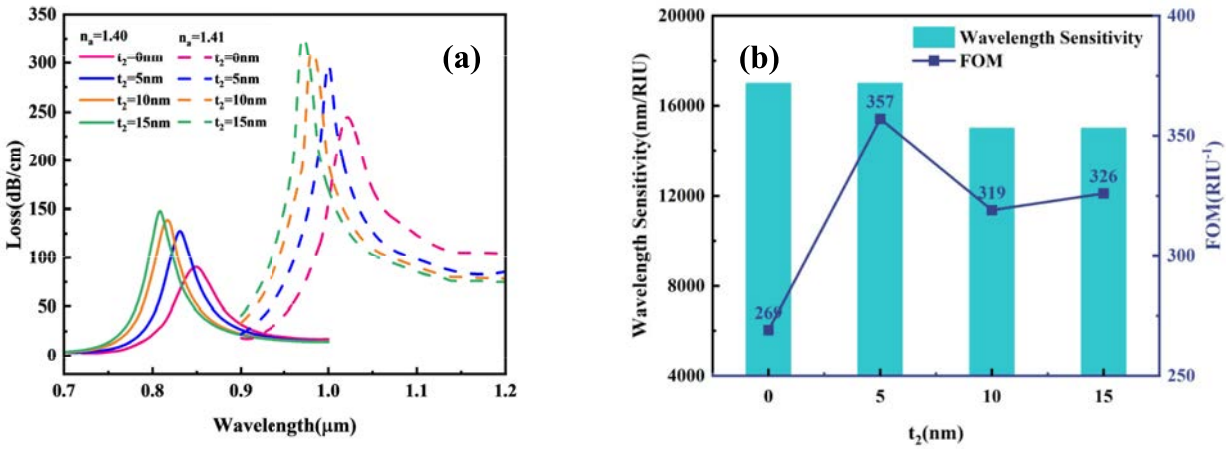

Fig. 7 **a** Loss spectra and **b** Wavelength sensitivity and FOM for different t_2

5 nm, Fig. 6a shows the loss spectra for different gold film thickness t_1. The loss spectra redshift as t_1 increases from 25 to 40 nm because the effective refractive index of the SPP mode increases with the thickness of the gold film, while the effective refractive index of the core mode remains unchanged. The phase matching point of the core mode and the SPP mode shifts toward longer wavelengths. Figure 6b compares the wavelength sensitivity and FOM for different gold film thicknesses. The wavelength sensitivity increases gradually with increasing t_1. However, the peak of the loss spectrum is relatively smaller for $t_1 = 40$ nm. It is because the thicker gold film increases the damping loss of the electric field and the SPR effect is weakened [34]. Therefore, the FWHM increases and FOM is lower. It means that the resolution of the sensor deteriorates. Therefore $t_1 = 35$ nm is selected as the optimal thickness. The influence of the ZnO film thickness t_2 on the sensing characteristics is analyzed. As shown in Fig. 7, the loss spectrum exhibits lower peak and wider FWHM without the ZnO layer ($t_2 = 0$ nm). With inserting the ZnO film the FWHM of the loss spectrum is reduced and FOM is enhanced. However, an excessively thick ZnO film decreases the wavelength sensitivity, as shown in Fig. 7b. When the thickness t_2 of the ZnO film is 5 nm, the sensor exhibits the optimal performance.

The large outer air holes with a diameter of d_3 affect the confining ability of the core mode. As d_3 decreases, the confinement to the core mode weakens, and the coupling between the core mode and the SPP mode is enhanced. Therefore, the peak of the loss spectrum increases as d_3

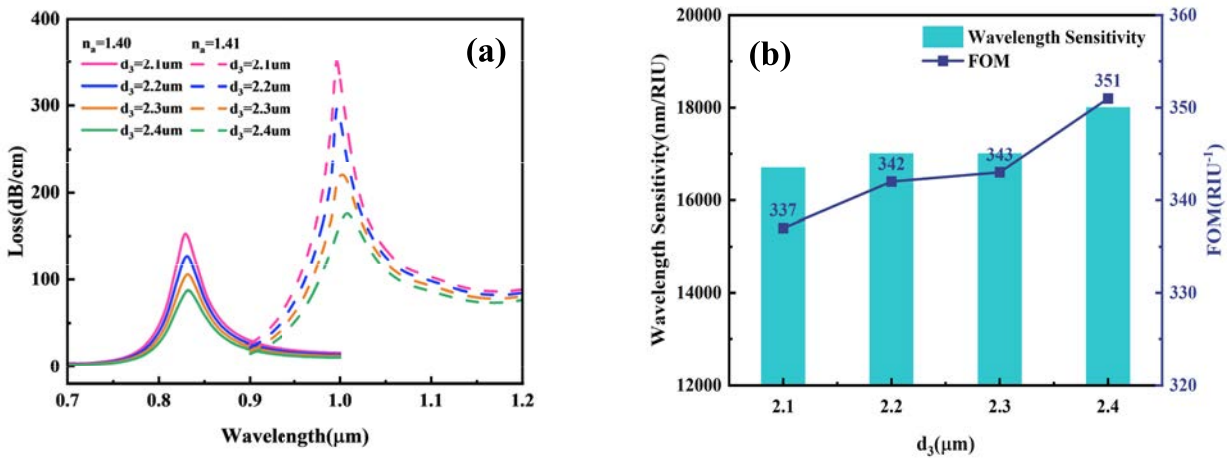

Fig. 8 **a** Loss spectra and **b** wavelength sensitivity and FOM for different d_3

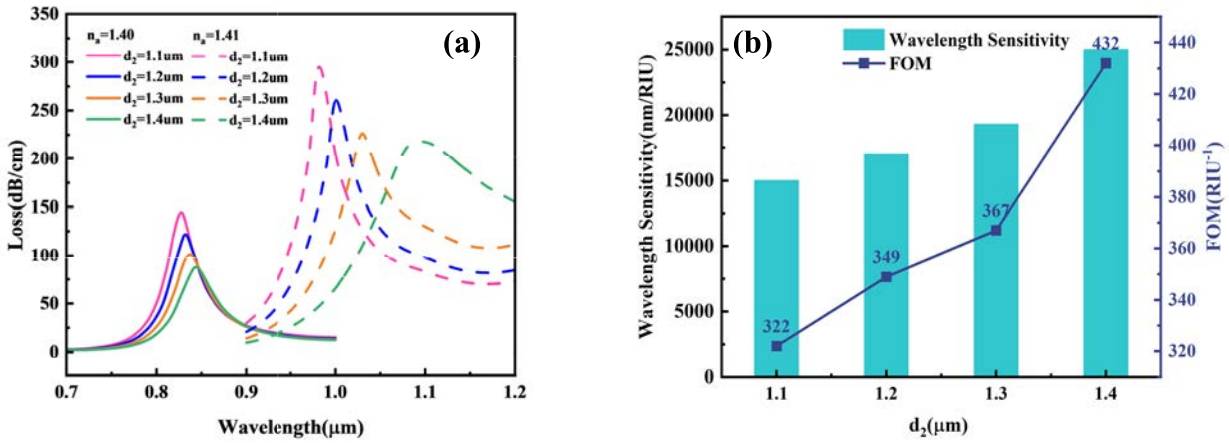

Fig. 9 **a** Loss spectra and **b** wavelength sensitivity and FOM for different d_2

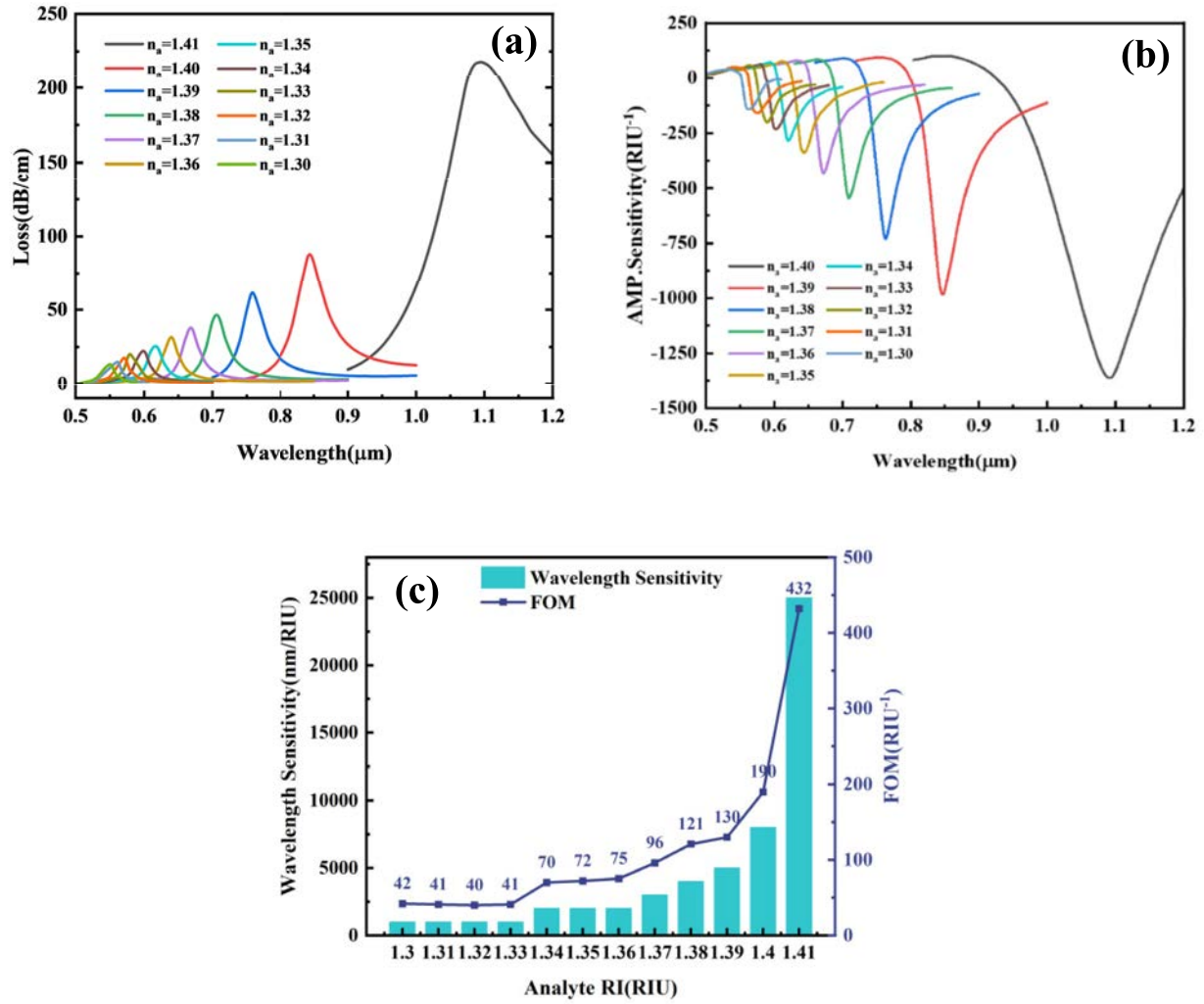

Fig. 10 **a** Loss spectra for different refractive indexes, **b** amplitude sensitivity, **c** wavelength sensitivity and FOM of the sensor in the measurement range of 1.30–1.41

Table 1 Performance comparison of groove-structured sensors

References	Coatings	RI Range	Max Wave. Sens. (nm/RIU)	Max FOM (RIU^{-1})
Ref. [21]	Au	1.17–1.40	13,000	/
Ref. [58]	Au	1.15–1.44	4520	230.56
Ref. [59]	MoS_2-Au	1.19–1.40	5100	29.143
Ref. [38]	Au	1.33–1.40	7000	94.97
Ref. [60]	Au	1.26–1.38	5626	/
This work	Au-ZnO	1.30–1.41	25,000	432

decreases from 2.4 μm to 2.1 μm, as shown in Fig. 8a. At the same time, a smaller d_3 decreases the effective refractive index of the core mode and the loss spectrum shifts to a shorter wavelength. Figure 8b compares the wavelength sensitivity and FOM for different d_3. It can be observed that $d_3 = 2.4$ μm is the optimal value.

Finally, the influence of the two air holes with a diameter of d_2 is analyzed. The two holes situated between the fiber core and the surface plasmonic substance form the coupling channel of the core mode and the SPP mode. Figure 9a shows the loss spectra for different diameters d_2. It is evident that the peak of the loss spectrum decreases as d_2 increases from 1.1 μm to 1.4 μm due to the narrow coupling channel and enhanced confinement ability to the core mode. Additionally, larger air holes result in the diminished effective refractive index of the core mode. Therefore, the loss spectra shift toward longer wavelengths. Figure 9b shows the wavelength sensitivity and FOM for different d_2, and the sensor delivers the optimal performance when $d_2 = 1.4$ μm.

According to above analysis, the optimal structural parameters of the PQF-SPR sensor are as follows: $d_1 = 1$ μm, $d_2 = 1.4$ μm, $d_3 = 2.4$ μm, $t_1 = 35$ nm, and $t_2 = 5$ nm. Figure 10a presents the loss spectra as the refractive indexes of the medium increase from 1.30 to 1.41. The peak of the loss spectra rise with the refractive indexes, while the resonance wavelengths redshift monotonically. The amplitude sensitivities for RI changes from 1.30 to 1.41 are presented in Fig. 10b, and the optimal amplitude sensitivity of 1360/RIU is obtained for $n_a = 1.40$. Figure 10c shows the wavelength sensitivity and FOM in this refractive index range. The maximum wavelength sensitivity is 25,000 nm/RIU with FOM of 432 RIU^{-1}. The average wavelength sensitivity is 4584 nm/RIU. If the spectrometer with a resolution of 0.1 nm is employed, the maximum resolution can reach 4×10^{-4} RIU. Then, we compared the sensing performance with various types of groove-structured PCF-SPR sensors reported in recent years. Table 1 verifies that the dual-groove dual-core PCF-SPR sensor proposed in this study exhibits superior sensing characteristics.

Conclusion

A novel dual-core PQF-SPR sensor comprising a ZnO–Au bilayer film is designed and analyzed. The sensor has a double-sided groove structure to enhance the SPR effect. The influence of the groove structure on the wavelength sensitivity and FOM is determined by the finite element method. By optimizing the PQF structure and thickness of the plasmonic layer, the groove-shape PQF-SPR sensor can be operated in the refractive index range of 1.30–1.41. Our analysis reveals that the optimized structure exhibits a maximum wavelength sensitivity and FOM of 25,000 nm/RIU and 432 RIU^{-1}, respectively. The results provide insights into the design of high-performance SPR sensors, and the structure discussed in this paper has large application potential in medical diagnostics, environmental monitoring, and biochemical sensing.

Acknowledgements This work was jointly supported by the Basic Research Support Project for the Excellent Youth Scholars of Heilongjiang Province [YQJH2023077], Hainan Province Science and Technology Special Fund [ZDYF2022GXJS222], Natural Science Foundation of Heilongjiang Province [JQ2023F001, LH2021F007], China Postdoctoral Science Foundation funded project [2020M670881], and City University of Hong Kong Donation Research Grants [DON-RMG 9229021 and 9220061].

Author Contribution Q.L. conceived and designed the study; L.L., K.W., and X.Z. conducted data collection and analysis; X.L. and Q.L. wrote the main manuscript text; X.Z., J.L., and W.L. prepared the figures; C.L., P.K.C., and Y.S. supervised the project and provided critical revisions. All authors reviewed and approved the final version of the manuscript.

Data Availability No datasets were generated or analysed during the current study.

Declarations

Conflict of interest The authors declare no competing interests.

References

1. Azab MY, Hameed MFO, Obayya SSA (2019) Temperature sensors based on plasmonic photonic crystal fiber. Comput Photonic Sens 179–201. https://doi.org/10.1007/978-3-319-76556-3_8
2. Kaziz S, Echouchene F, Gazzah MH (2024) Optimizing PCF-SPR sensor design through Taguchi approach, machine learning, and genetic algorithms. Sci Rep 14:7837. https://doi.org/10.1038/s41598-024-55817-9
3. Falah AAS, Wong WR, Mahdiraji GA et al (2024) D-shaped PCF with quasi-sinusoidal surface topography for dual-polarization and enhanced performance surface plasmon resonance

sensor. J Lightwave Technol. https://doi.org/10.1109/JLT.2024.3366331
4. Tong R, Zhao K, Xing B et al (2024) An optical fiber sensor for salinity and temperature simultaneous detection based on dual SPR effect. Opt Laser Technol 175:110760. https://doi.org/10.1016/j.optlastec.2024.110760
5. Wang Y, Huang Q, Zhu W et al (2018) Novel optical fiber SPR temperature sensor based on MMF-PCF-MMF structure and gold-PDMS film. Opt Express 26:1910–1917. https://doi.org/10.1364/OE.26.001910
6. De I, Gaur A, Rastogi V (2024) Multimode erbium-doped fiber amplifier based on double-clad GeO_2-doped photonic crystal fiber supporting 38 orbital angular momentum modes. J Lightwave Technol. https://doi.org/10.1109/JLT.2024.3395835
7. Almawgani AHM, Mollah MA, Adam YS et al (2025) High-performance optical fiber biosensor for early cancer cell identification. Plasmonics. https://doi.org/10.1007/s11468-025-03004-5
8. Shafi ABMA, Al-Tabatabaie KF, Abdulrazak LF et al (2025) Exposed core fiber plasmonics biosensor for SARS-CoV-2 particle detection. Plasmonics. https://doi.org/10.1007/s11468-025-02955-z
9. Mollah MA, Abdulrazak LF, Tabassum T et al (2025) Photonic crystal fiber plasmonic biosensor for SARS-CoV-2 particle quantification and detection. Plasmonics. https://doi.org/10.1007/s11468-025-02840-9
10. Deepti MR, Mollah MA (2025) PCF-based multi-analyte refractive index sensor for pathogen detection in water. J Comput Electron 24:28. https://doi.org/10.1007/s10825-024-02239-5
11. Ali YAA, Rahman A, Almawgani AHM et al (2025) Internal sensing with exposed core fiber plasmonic sensor and machine-learning approach for RI prediction. Plasmonics (in press). https://doi.org/10.1007/s11468-024-02754-y
12. Liu Q, Wang K, Sun Y et al (2024) Surface plasmon resonance methane sensor based on the D-type photonic quasi-crystal fiber with double-layer films. Opt Fiber Technol 84:103779. https://doi.org/10.1016/j.yofte.2024.103779
13. Yang XY, Chen HN, Yue LJ et al (2025) Surface engineering of 1D Na-doped Pd/WO_3 nanorods for chemiresistive H_2 sensing. Sens Actuators B Chem 423:136825. https://doi.org/10.1016/j.snb.2024.136825
14. Zhang Q, Li J (2024) Performance demonstration of ammonia sensor based on cascaded-splice PCF. IEEE Sens J. https://doi.org/10.1109/jsen.2024.3454272
15. Goyal AK, Pal S (2020) Design analysis of Bloch surface wave based sensor for haemoglobin concentration measurement. Appl Nanosci 10:3639–3647. https://doi.org/10.1007/s13204-020-01437-4
16. Goyal AK, Saini J (2020) Performance analysis of Bloch surface wave-based sensor using transition metal dichalcogenides. Appl Nanosci 10:4307–4313. https://doi.org/10.1007/s13204-020-01538-0
17. Gonzalez-Valencia E, Herrera RA, Torres P (2019) Bloch surface wave resonance in photonic crystal fibers: towards ultra-wide range refractive index sensors. Opt Express 27:8236–8245. https://doi.org/10.1364/OE.27.008236
18. Yi H, Goyal AK, Massoud Y (2024) Performance optimization of Bloch surface wave based devices using an XGBoost machine learning model. Opt Continuum 3:693–703. https://doi.org/10.1364/optcon.520638
19. Gonzalez-Valencia E, Villar ID, Torres P (2021) Novel Bloch wave excitation platform based on few-layer photonic crystal deposited on D-shaped optical fiber. Sci Rep 11:11266. https://doi.org/10.1038/s41598-021-90504-z
20. Alabsi BA, Mollah MA, Almawgani AHM et al (2025) Convex analyte channel photonic crystal fiber plasmonic sensor and RI prediction incorporating machine learning approach. Plasmonics (in press). https://doi.org/10.1007/s11468-025-02781-3
21. Srivastava R, Kumar V, Prajapati YK (2024) Highly sensitive SPR based PCF sensor for broader analyte detection range including blood compositions detection. Optik 314:172010. https://doi.org/10.1016/j.ijleo.2024.172010
22. Li K, Yin Z, Wang C et al (2024) Enhancement of SPR effect and sensing characteristics in photonic crystal fiber with $Ti_3C_2T_x$-Mxene/silver film. J Lightwave Technol. https://doi.org/10.1109/JLT.2024.3365956
23. Li K, Li S, Du H (2024) Near-infrared PCF sensor with ultra-high sensitivity detection based on surface plasmon resonance. J Lightwave Technol. https://doi.org/10.1109/jlt.2024.3489581
24. Sardar MR, Faisal M (2024) Dual-core dual-polished PCF-SPR sensor for cancer cell detection. IEEE Sens J 24:9843–9854. https://doi.org/10.1109/JSEN.2024.3358173
25. Divya J, Selvendran S, Raja AS, Chitra K (2024) Silver-TiO_2 coated D-shaped photonic crystal fiber based SPR sensor for ultrasensitive refractive index detection: design and FEM analysis. Phys Scr 99:025505. https://doi.org/10.1088/1402-4896/ad1864
26. Luo W, Li X, Abbasi SA et al (2023) Analysis of the D-shaped PCF-based SPR sensor using resonance electron relaxation and Fourier domain method. Opt Lasers Eng 166:107588. https://doi.org/10.1016/j.optlaseng.2023.107588
27. Ma Y, Liu F, Ren Q et al (2023) Dual-band highly-sensitive SPR photonic crystal fiber sensor based on birefringence analysis. Opt Commun 532:129253. https://doi.org/10.1016/j.optcom.2022.129253
28. Liu Q, Jiang Y, Sun Y et al (2021) Surface plasmon resonance sensor based on U-shaped photonic quasi-crystal fiber. Appl Opt 60:1761–1766. https://doi.org/10.1364/ao.419518
29. You Q, Pan H, Zhao Z et al (2024) Highly sensitive wide detection range semicircular convex slot PCF temperature sensor based on surface plasmon resonance. IEEE Sens J. https://doi.org/10.1109/JSEN.2024.3422688
30. Liu Q, Sun J, Sun Y et al (2020) High-sensitivity SPR sensor based on eight-fold eccentric core PQF with locally coated indium tin oxide. Appl Opt 59:5484–5489. https://doi.org/10.1364/ao.395605
31. Ibrahimi KM, Kumar R, Pakhira W (2023) Enhance the design and performance analysis of a highly sensitive twin core PCF SPR biosensor with gold plating for the early detection of cancer cells. Plasmonics 18:995–1006. https://doi.org/10.1007/s11468-023-01825-w
32. Sakib MN, Hossain MB, Al-tabatabaie KF et al (2019) High performance dual core D-shape PCF-SPR sensor modeling employing gold coat. Results Phys 15:102788. https://doi.org/10.1016/j.rinp.2019.102788
33. Wang H, Wu M, Zheng S et al (2023) Surface plasmon resonance sensor based on seven-core photonic crystal fiber for refractive index and temperature measurement. Opt Laser Technol 164:109511. https://doi.org/10.1016/j.optlastec.2023.109511
34. Anik MHH, Islam SMR, Talukder H et al (2021) A highly sensitive quadruple D-shaped open channel photonic crystal fiber plasmonic sensor: a comparative study on materials effect. Results Phys 23:104050. https://doi.org/10.1016/j.rinp.2021.104050
35. Anik MHH, Isti MIA, Islam SMR et al (2020) Milled microchannel-assisted open D-channel photonic crystal fiber plasmonic biosensor. IEEE Access 9:2924–2933. https://doi.org/10.1109/ACCESS.2020.3047509
36. Isti MIA, Anik MHH, Nuzhat S et al (2022) Highly sensitive double D-shaped channel photonic crystal fiber based plasmonic refractive index sensor. Opt Continuum 1:575–590. https://doi.org/10.1364/optcon.452020

37. Rahman MDT, Datto S, Nazmussakib MD (2023) Highly sensitive circular slotted gold-coated micro channel photonic crystal fiber based plasmonic biosensor. OSA Continuum 4:1808–1826. https://doi.org/10.1364/osac.425279
38. Islam N, Arif MFH, Yousuf MA et al (2023) Highly sensitive open channel based PCF-SPR sensor for analyte refractive index sensing. Results Phys 46:106266. https://doi.org/10.1016/j.rinp.2023.106266
39. Gao S, Wei K, Yang H et al (2023) Design of surface plasmon resonance-based D-type double open-loop channels PCF for temperature sensing. Sensors 23:7569. https://doi.org/10.3390/s23177569
40. Majeed MF, Ahmad AK (2024) Design and analysis of a high sensitivity open microchannel PCF-based surface plasmon resonance refractometric sensor. Opt Mater 147:114617. https://doi.org/10.1016/j.optmat.2023.114617
41. Mittal S, Saharia A, Ismail Y et al (2023) Design and performance analysis of a novel hoop-cut SPR-PCF sensor for high sensitivity and broad range sensing applications. IEEE Sens J 24:2697–2704. https://doi.org/10.1109/JSEN.2023.3339813
42. Dai T, Yan J, Zhu W et al (2024) Ultra-high sensitivity surface plasmon U-channel photonic crystal fiber for hemoglobin sensing. Sens Actuators A Phys 366:115053. https://doi.org/10.1016/j.sna.2024.115053
43. Liu Q, Wang K, Sun Y et al (2024) Two-core photonic quasicrystal fiber - surface plasmon resonance (PQF-SPR) methane sensor comprising the ZnO/Au composite film: design and FEM simulation. Phys Scr 99:125518. https://doi.org/10.1088/1402-4896/ad85ff
44. Bertoncini A, Liberale C (2020) 3D printed waveguides based on photonic crystal fiber designs for complex fiber-end photonic devices. Optica 7:1487–1494. https://doi.org/10.1364/optica.397281
45. Yuan L, Huang J, Lan X et al (2014) All-in-fiber optofluidic sensor fabricated by femtosecond laser assisted chemical etching. Opt Lett 39:2358–2361. https://doi.org/10.1364/OL.39.002358
46. Micco A, Ricciardi A, Pisco M et al (2015) Optical fiber tip templating using direct focused ion beam milling. Sci Rep 5:15935. https://doi.org/10.1038/srep15935
47. Song H, Wu H, Xu Y et al (2025) MSM fiber optic surface plasmon resonance glucose sensor based on SnO_2 nanofibers/Au structure. Photonics Sens 15:250119. https://doi.org/10.1007/s13320-024-0733-1
48. Karki B, Trabelsi Y, Pal A et al (2024) Direct detection of dopamine using zinc oxide nanowire-based surface plasmon resonance sensor. Opt Mater 147:114555. https://doi.org/10.1016/j.optmat.2023.114555
49. Dogan Y, Erdogan I (2023) Highly sensitive MoS_2/graphene based D-shaped optical fiber SPR refractive index sensor with Ag/Au grated structure. Opt Quantum Electron 55:1066. https://doi.org/10.1007/s11082-023-05315-5
50. Ghosh G, Endo M, Iwasaki T (1994) Temperature-dependent Sellmeier coefficients and chromatic dispersions for some optical fiber glasses. J Lightwave Technol 12:1338–1342. https://doi.org/10.1109/50.317500
51. Vial A, Grimault A-S, Macías D et al (2005) Improved analytical fit of gold dispersion: application to the modeling of extinction spectra with a finite-difference time-domain method. Phys Rev B 71:085416. https://doi.org/10.1103/PhysRevB.71.085416
52. Kaur V, Singh S (2020) Design of D-shaped PCF-SPR sensor with dual coating of ITO and ZnO conducting metal oxide. Optik 220:165135. https://doi.org/10.1016/j.ijleo.2020.165135
53. Liu EX, Liang SW, Liu JJ (2019) Double-cladding structure dependence of guiding characteristics in six-fold symmetric photonic quasi-crystal fiber. Superlattices Microstruct 130:61–67. https://doi.org/10.1016/j.spmi.2019.03.011
54. Liu C, Yang L, Liu Q et al (2017) Analysis of a surface plasmon resonance probe based on photonic crystal fibers for low refractive index detection. Plasmonics 13:779–784. https://doi.org/10.1007/s11468-017-0572-7
55. Haque E, Hossain MA, Ahmed F et al (2018) Surface plasmon resonance sensor based on modified D-shaped photonic crystal fiber for wider range of refractive index detection. IEEE Sens J 18:8287–8293. https://doi.org/10.1109/JSEN.2018.2865514
56. Islam MS, Cordeiro CM, Sultana J et al (2019) A Hi-Bi ultrasensitive surface plasmon resonance fiber sensor. IEEE Access 7:79085–79094. https://doi.org/10.1109/ACCESS.2019.2922663
57. Gauvreau B, Hassani A, Fehri MF et al (2007) Photonic bandgap fiber-based surface plasmon resonance sensors. Opt Express 15:11413–11426. https://doi.org/10.1364/OE.15.011413
58. Muqeet A, Ashraf MA, Mumtaz F (2024) Spatially tuned photonic crystal fiber sensor mimics visible and near-infrared regimes for wide-range multi-analyte detection. Measurement 227:114272. https://doi.org/10.1016/j.measurement.2024.114272
59. Guo X, Wang Y, Sang T et al (2023) SPR sensor based on a concave photonic crystal fiber structure with MoS_2/Au layers. Materials 16:5523. https://doi.org/10.3390/ma16165523
60. Pan H, Pan F, Zhang A et al (2022) Wide refractive index detection range surface plasmon resonance sensor based on D-shaped photonic crystal fiber. Opt Quantum Electron 54:393. https://doi.org/10.1007/s11082-022-03805-6